Chinese Chemical Letters 33 (2022) 2959–2964

Contents lists available at ScienceDirect

Chinese Chemical Letters

journal homepage: www.elsevier.com/locate/cclet

Tumor microenvironment-responsive $MnSiO_3$-Pt@BSA-Ce6 nanoplatform for synergistic catalysis-enhanced sonodynamic and chemodynamic cancer therapy

Fan Jiang[a,b], Chunzheng Yang[a,b], Binbin Ding[a,b], Shuang Liang[a,b], Yajie Zhao[a,b], Ziyong Cheng[a,b], Min Liu[c], Bengang Xing[d], Ping'an Ma[a,b,*], Jun Lin[a,b,*]

[a] State Key Laboratory of Rare Earth Resource Utilization, Changchun Institute of Applied Chemistry, Chinese Academy of Sciences, Changchun 130022, China
[b] School of Applied Chemistry and Engineering, University of Science and Technology of China, Hefei 230026, China
[c] Department of Periodontology, Stomatological Hospital, Jilin University, Changchun 130021, China
[d] School of Physical & Mathematical Sciences, Nanyang Technological University, Singapore 639798, Singapore

ARTICLE INFO

Article history:
Received 14 September 2021
Revised 17 December 2021
Accepted 31 December 2021
Available online 7 January 2022

Keywords:
Sonodynamic therapy
Chemodynamic therapy
Artificial enzyme
Oxygen generation
Synergetic therapy

ABSTRACT

Compared with traditional photodynamic therapy (PDT), ultrasound (US) triggered sonodynamic therapy (SDT) has a wide application prospect in tumor therapy because of its deeper penetration depth. Herein, a novel $MnSiO_3$-Pt (MP) nanocomposite composed of $MnSiO_3$ nanosphere and noble metallic Pt was successfully constructed. After modification with bovine serum albumin (BSA) and chlorine e6 (Ce6), the multifunctional nanoplatform $MnSiO_3$-Pt@BSA-Ce6 (MPBC) realized the magnetic resonance imaging (MRI)-guided synergetic SDT/chemodynamic therapy (CDT). In this nanoplatform, sonosensitizer Ce6 can generate singlet oxygen ($^1O_2$) to kill cancer cells under US irradiation. Meanwhile, the loaded Pt has the ability to catalyze the decomposition of overexpressed hydrogen peroxide (H_2O_2) in tumor microenvironment (TME) to produce oxygen (O_2), which can conquer tumor hypoxia and promote the SDT-induced $^1O_2$ production. In addition, MP can degrade in mildly acidic and reductive TME, causing the release of Mn^{2+}. The released Mn^{2+} not only can be used for MRI, but also can generate hydroxyl radical (•OH) for CDT by Fenton-like reaction. The multifunctional nanoplatform MPBC has high biological safety and good anticancer effect, which displays the great latent capacity in biological application.

In recent years, external minimally invasive or noninvasive treatment methods have attracted much attention worldwide due to its spatial/temporal controllability, tumor specificity, and low toxicity [1–3]. Among them, photodynamic therapy (PDT), a treatment method that can induce cell death by stimulating photosensitizers to produce cytotoxic reactive oxygen species (ROS) under laser irradiation, has been widely explored [4–7]. However, the low penetrating depth of light hinders the therapeutic effect. Lately, ultrasound (US) has become the research hotspot because of its noninvasiveness, low cost, and high depth of tissue penetration. It has been reported that US can activate sonosensitizers to produce toxic ROS for tumor treatment, which is termed as sonodynamic therapy (SDT) [8–11]. In the process of SDT, oxygen (O_2) is beneficial to singlet oxygen ($^1O_2$) generation. But the severe hypoxia in the solid tumor microenvironment (TME) and the O_2 consumption during SDT restrict the therapeutic efficacy of SDT [12–14]. Therefore, increasing the content of oxygen in TME can effectively enhance the treatment effect of SDT. Aroused by this, many efforts have been made. Some O_2 storage materials, such as metal–organic frameworks [15–17], hemoglobin [18–21], perfluorocarbon [22–24], have been reported to increase the content of O_2 in TME. In addition, some nanozymes can also be widely utilized to increase O_2 content by *in situ* O_2 generation, mainly including Pt [25–27], MnO_2 [28–30], CeO_2 [31–33], and so on.

Chemodynamic therapy (CDT) is considered as an attractive way for cancer treatment by generating excessive hydroxyl radicals (•OH) for cancer cell apoptosis [34]. Some metal (iron [35–37], copper [38–41], manganese [42–44]) ions have been reported to catalyze hydrogen peroxide (H_2O_2) in TME to produce •OH. Generally, the body has the natural metal ions (*i.e.*, Fe ion) to produce •OH by catalyzing the decomposition of H_2O_2 *via* the Fenton reaction. However, the efficiency of Fenton reaction is decreased due to the low content of Fe ions in cancer cells. Therefore, adding additional CDT reagent is of great significance to promote the formation of toxic •OH. Unfortunately, CDT alone is difficult to obtain ideal therapeutic effect. To solve this problem, CDT is usually combined with other treatment methods. Lin *et al.* integrated CaO_2

* Corresponding authors.
E-mail addresses: mapa675@ciac.ac.cn (P. Ma), jlin@ciac.ac.cn (J. Lin).

https://doi.org/10.1016/j.cclet.2021.12.096
1001-8417/

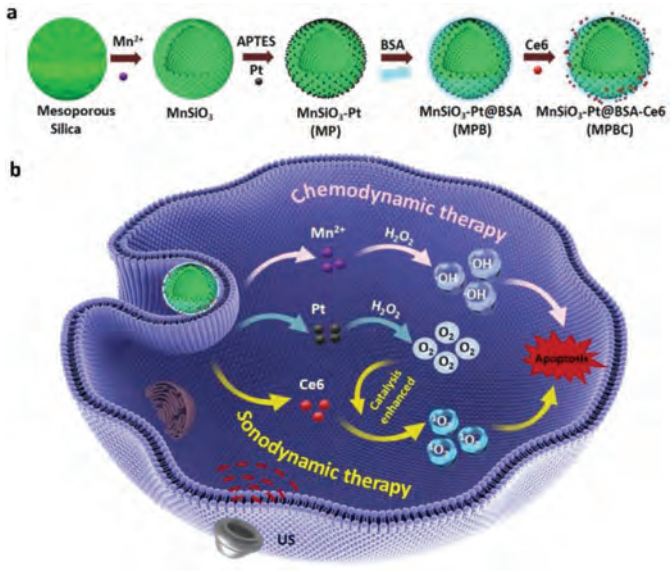

Scheme 1. (a) Schematic illustration for the synthesis steps of MPBC nanoplatform. Mesoporous silica was treated by hydrothermal treatment to produce $MnSiO_3$. Pt NPs were absorbed on the surface of amino-modified $MnSiO_3$. BSA was modified to improve the biocompatibility of NPs. Then sonosensitizer Ce6 was conjugated with MPB through the formation of amide bond. (b) The antitumor mechanism of MPBC nanoplatform. Under US irradiation, Ce6 could generate ROS for SDT. And the O_2 in TME generated by the catalase-like activity of the loaded Pt could improve the SDT effect. Meanwhile, the released Mn^{2+} by degradation of NPs could catalyze H_2O_2 to produce •OH for CDT, causing the good synergistic therapeutic effects of SDT and CDT.

nanodots and Fe^{3+} co-incorporated MOF to realize the combined Radiotherapy (RT)/CDT [37]. Liang *et al.* synthesized platinum (IV) prodrug-conjugated albumin-based CuO/MnO_x nanoagent for combined chemotherapy/CDT [45]. Jia *et al.* developed an intelligent nanoplatform by immobilizing UCNPs on FeMn-LDH nanosheets for synergistic photothermal/photodynamic/CDT [46]. Therefore, it is promising to combine CDT with other treatment modalities for cancer therapy.

Inspired by above finding, herein, we first synthesized platinum (Pt)-modified $MnSiO_3$ nanocomposite. After modification with bovine serum albumin (BSA) and chlorine e6 (Ce6), the multifunctional nanoplatform $MnSiO_3$-Pt@BSA-Ce6 (MPBC) was successfully constructed for catalysis-enhanced SDT/CDT. Under US irradiation, Ce6 can convert O_2 into $^1O_2$ for SDT to kill tumor cells. $MnSiO_3$ is sensitive to the weak acidity and high GSH content in the TME, causing the rapid release of Mn^{2+}. The released Mn^{2+} not only could generate •OH for CDT by catalyzing the endogenic H_2O_2, but also displayed an excellent T_1-weighted MRI performance. Besides, the metal Pt can catalyze the H_2O_2 in TME into O_2 to overcome tumor hypoxia and accelerate the SDT-induced ROS generation. *In vitro* and *in vivo* experiments proved that the nanoplatform had a remarkable therapeutic effect, which had enormous potential in cancer treatment.

In this work, we first synthesized uniform $MnSiO_3$ nanosphere. Then polyvinylpyrrolidone (PVP) decorated Pt nanoparticles (NPs) were absorbed on the surface of amino-modified $MnSiO_3$. The formed MP was decorated with BSA to improve the biocompatibility of NPs. After conjugating sonosensitizer Ce6 with MPB through the formation of amide bonds, the multifunctional nanoplatform was successfully constructed. Scheme 1 displayed the schematic summary of the detailed synthesis procedures and therapeutic mechanism of the nanoplatform. The $MnSiO_3$ nanospheres with an average diameter of 120 nm were prepared based on well-dispersed mesoporous silica nanoparticles by a hydrothermal method (Figs. 1a and b). Meanwhile, the PVP coated-Pt NPs with an average diameter of 4 nm were also successfully prepared (Fig. 1c). After $MnSiO_3$ was modificated with 3-aminopropyltriethoxysilane (APTES), the Pt NPs were decorated onto the surface of $MnSiO_3$ to form MP NPs by electrostatic adsorption. Transmission electron microscope (TEM) images (Fig. 1d) and X-ray diffraction (XRD) (Fig. 1f) pattern proved the successful construction of MP NPs. The nitrogen adsorption-desorption isotherm curves were displayed in Fig. 1h. Compared with $MnSiO_3$ (198.9 m^2/g, black), the specific surface areas of MP (142.2 m^2/g, red) obviously decreased, and the corresponding pore size also decreased. These results were attributed to the blockage of $MnSiO_3$ channel by Pt NPs. The Energy dispersive X-ray (EDX) mapping (Fig. 1e) and X-ray photo-electron spectroscopy (XPS) (Fig. S1 in Supporting information) confirmed the elemental compositions of MP NPs. In Fig. 1g, the high resolution XPS demonstrated that the Mn $2p_{3/2}$ was composed of Mn^{2+} (641 eV), Mn^{3+} (642 eV), and Mn^{4+} (644 eV). BSA was adsorbed on the surface of MP NPs to improve the biocompatibility. Fourier transform infrared (FTIR) spectra demonstrated the successful loading of BSA (Fig. S2 in Supporting information). The absorption bands of MPB around 1655 and 1532 cm^{-1} belonged to the amide I and amide II bands of BSA, respectively [47]. Thermogravimetric analysis (TGA) showed that the content of BSA loaded on MP was 17% (Fig. 2a). Sonosensitizer molecule Ce6 was linked on the surface of MPB though the amidation reaction between the amino group of BSA and carboxyl group of Ce6. The absorption peaks of Ce6 (404 and 660 nm) were all observed in the absorption spectrum of MPBC (Fig. 2b), demonstrating the successful loading of Ce6. The loading content of Ce6 was estimated to be 20% by UV−vis absorption spectra (Fig. S3 in Supporting information). The change of zeta potential on the surface of NPs displayed the every procedure of preparation process (Fig. 2c).

Iron-triggered Fenton chemistry has been widely used to induce tumor cells apoptosis though catalyzing endogenous H_2O_2 into •OH. It is reported that the Mn^{2+} also can achieve CDT by generating •OH through Fenton-like reaction [48,49]. Here, we chose methylene blue (MB), a dye that can be degraded by •OH, as an indicator to verify the •OH generation. As shown in Fig. 2d, bicarbonate (HCO_3^-) plays an important role in Mn^{2+}-mediated Fenton-like reaction. Meanwhile, the •OH generation is proportional to the concentration of H_2O_2 (Fig. 2e). With the increase of H_2O_2 concentration, the absorbance of MB decreased, confirming more •OH generation.

Metal Pt has been reported as an artificial enzyme to generate O_2 by decomposing H_2O_2. Compared with natural enzymes, artificial enzymes possess following advantages: low cost, good stability, and ease preparation [50–52]. To investigate the catalase-like activity of MP, we employed a dissolved oxygen instrument to monitor the O_2 generation. As displayed in Fig. 2f, in the absence of MP, the O_2 concentration of the solution remained stable, demonstrating that the influence of the environment on the measurement results was negligible. When adding MP into the solution, O_2 was released rapidly within a short time, confirming the excellent catalytic ability of MP. Sufficient O_2 supply is conducive to the $^1O_2$ generation. Here, singlet oxygen sensor green (SOSG), a dye that is highly specific to $^1O_2$, was employed to explore the $^1O_2$ generation ability of MPBC under US irradiation. As shown in Fig. 2g, the fluorescent signals of the MPBC group dramatically increased with the increase of US time, proving the SDT effect of MPBC. Besides, the generation of $^1O_2$ is dependent on the power density of US irradiation (Fig. 2h). More importantly, the presence of H_2O_2 could greatly promote the $^1O_2$ yield induced by US irradiation (Fig. 2i), which was because the MP could generate sufficient O_2 to enhance $^1O_2$ production by catalyzing H_2O_2 under US irradiation.

To explore the therapeutic mechanism *in vitro*, we first evaluated the intracellular uptake of MPBC by flow cytometry (FCM).

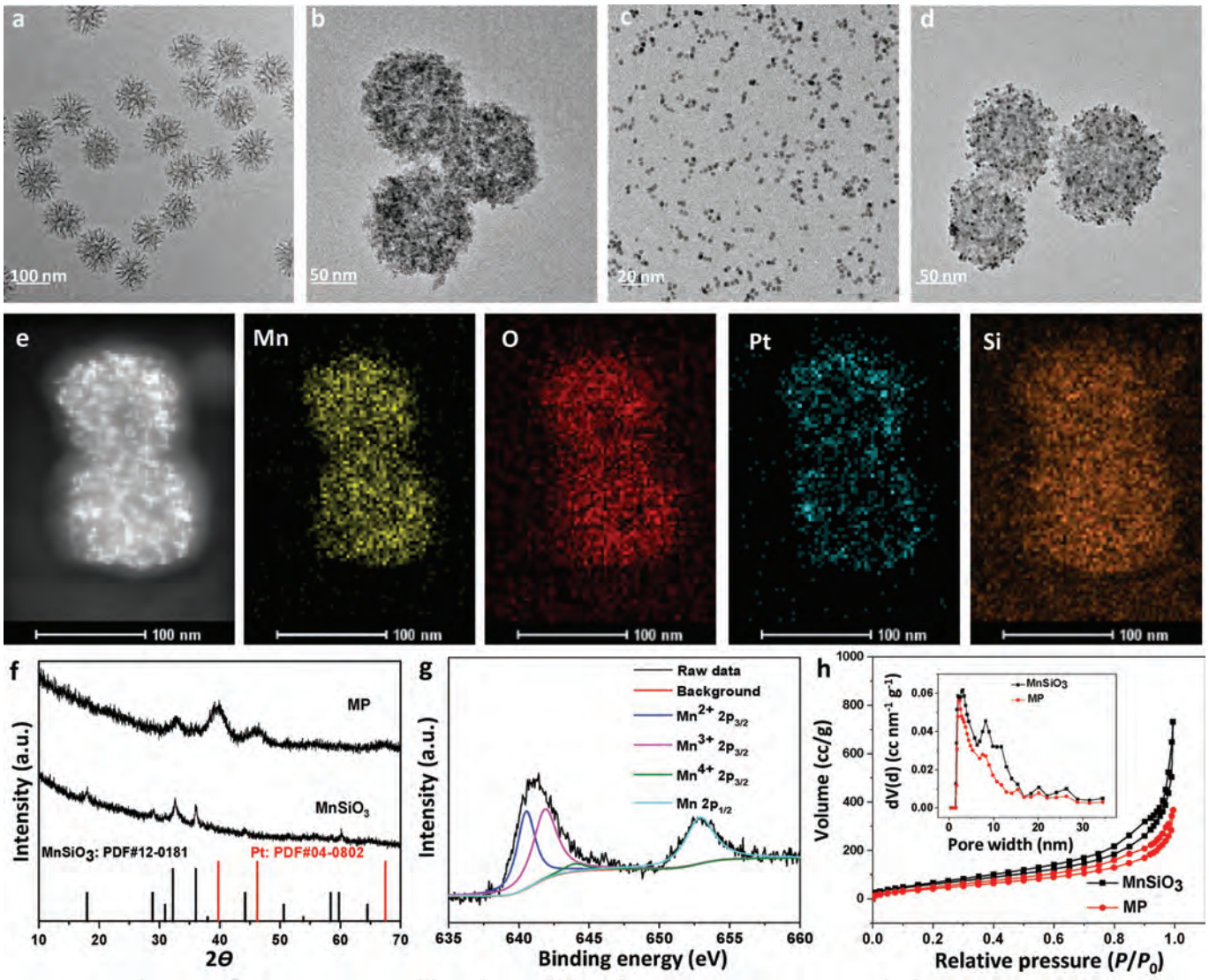

Fig. 1. TEM images of (a) Mesoporous silica, (b) $MnSiO_3$ spheres, (c) PVP-Pt NPs, and (d) MP NPs. (e) The EDS and elemental mappings of MP. (f) XRD spectra of $MnSiO_3$ and MP. (g) High-resolution Mn 2p XPS spectra of MP. (h) N_2 adsorption-desorption isotherm and pore size distribution (inset image) of $MnSiO_3$ (black) and MP (red).

As depicted in Fig. 3a, NPs could be effectively internalized by cells as the coincubation time extended. Then, the biocompatibility of MPB *in vitro* was evaluated by cell counting kit-8 (CCK-8) assay. As shown in Fig. S4 (Supporting information), cells treated with MPB NPs displayed 85% survival rate on fibroblast cell lines (L929) cells when the concentration of MPB was 100 ppm, indicating the excellent biocompatibility of MPB NPs. Meanwhile, the killing effect of MP NPs on human cervix cancer cells (HeLa) cells was higher than that of normal cells, which was due to the more •OH production *via* Mn^{2+}-mediated Fenton-like reaction in cancer cells [53,54]. In addition, bis(triphenylphosphine) ruthenium(II) dicarbonyl chloride ($[Ru(dpp)_3]Cl_2$) was used to evaluate the catalytic O_2 production capacity of MPB. As shown in Fig. S5 (Supporting information), the fluorescence intensity of MPB group is weaker than that of control group, suggesting more O_2 generation. FCM experiment also proved the result (Fig. 3b). Then we employed 2′,7′-dichlorofluorescein diacetate (DCFH-DA), a dye that could be rapidly oxidized to bright green fluorescence 2,7-dichlorofluorescein (DCF) by ROS, to studied the intracellular ROS production. As shown in Fig. 3d, the MPB group showed a weak green fluorescence compared with the control and US groups, which was attributed to the Mn^{2+}-mediated Fenton-like reaction. Especially, the cells treated with MPBC combined with US irradiation displayed the strongest green fluorescence, which was because Pt catalyzed the decomposition of endogenous H_2O_2 into O_2 for promoting US-triggered ROS generation. Next, we explored the synergistic effect of MPBC. The cells were divided into six groups, such as the control group, US group, MPB group, MPB + US group, MPBC group and MPBC + US group. From Fig. 3c, compared with the control group, US group showed negligible cell damage. It is noteworthy that the cell viability of MPBC + US group was lower than that of the other groups, demonstrating the good anticancer effect of combined catalysis-enhanced SDT and CDT. Furthermore, we also carried out FCM experiments to study the anticancer effect of combined CDT/SDT. In Fig. 3e, the MPBC + US group displayed the highest percentage of cell apoptosis compared with other groups. The live/dead staining assay also confirmed the extensive cell death of MPBC + US group (Fig. S6 in Supporting information). The above results demonstrate that the MPBC-based combined CDT/SDT have a good ability to kill cancer cells and possess a great potential in cancer therapy.

Motivated by the good anti-cancer effect of MPBC *in vitro*, the therapeutic efficacy of MPBC *in vivo* was then explored. We randomly divided the U14 tumor-bearing Balb/c mice into six groups: (1) control; (2) US; (3) MPB; (4) MPB + US; (5) MPBC; (6) MPBC + US. The mice were injected with NPs intratumorally. Af-

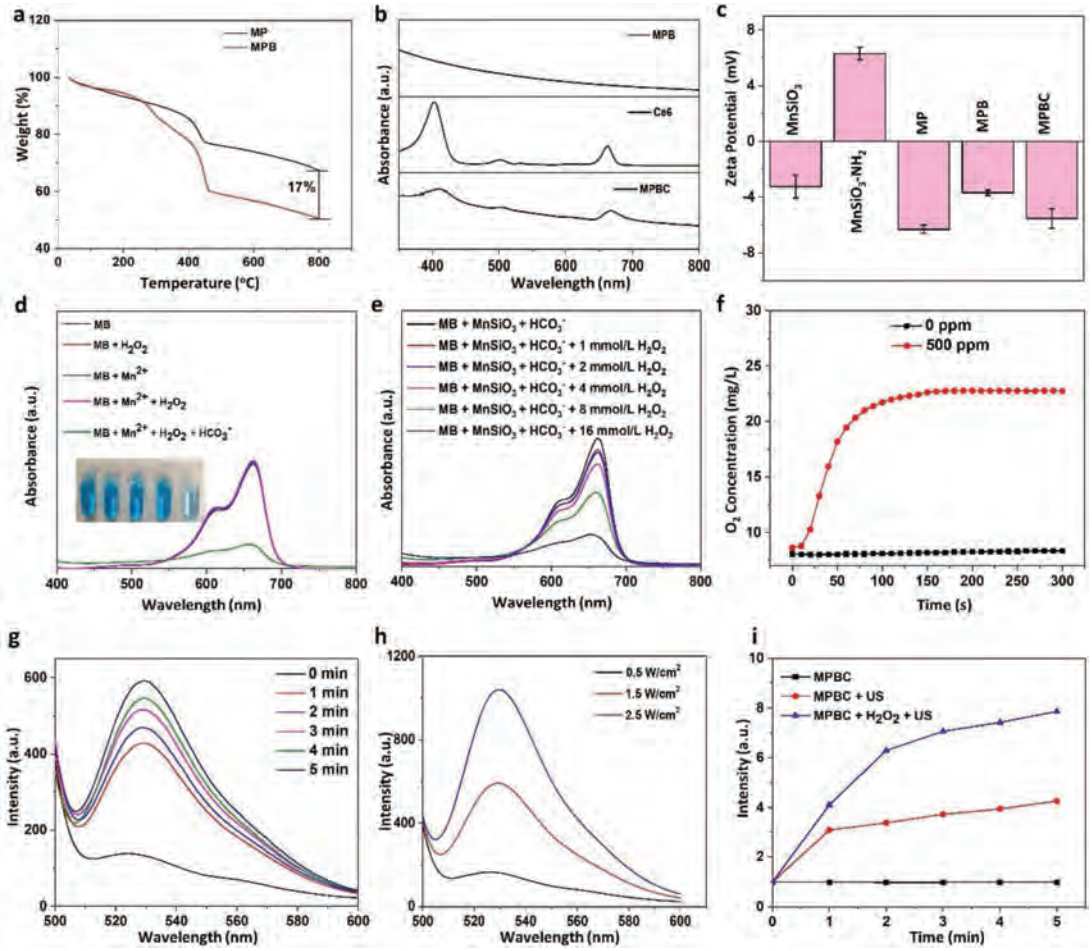

Fig. 2. (a) TGA of MP and MPB. (b) UV–vis–NIR absorption spectra of MPB, free Ce6, and MPBC. (c) Zeta potential of NPs in each synthesis step. (d) The absorption spectra of MB in different solutions (25 mmol/L $NaHCO_3$/5% CO_2 buffer solution, 10 μg/mL MB, 8 mmol/L H_2O_2, and 0.5 mmol/L $MnCl_2$). (e) The absorption spectra of MB in different H_2O_2 concentrations. (f) The O_2 production in H_2O_2 solution (1 mmol/L). (g) The fluorescence intensities of SOSG in MPBC solution under US irradiation. (h) The fluorescence intensities of SOSG in MPBC solution under different US irradiation densities for 5 min. (i) The production of $^1O_2$ in MPBC solution at different conditions.

ter 3 h post-injection of NPs (15 mg/kg), mice were exposed to US irradiation (1.0 MHz, 1.5 W/cm^2, 50% duty cycle, 5 min). The tumor sizes and weights of mice were measured every two days after treatment. As displayed in Fig. 4a and Fig. S7 (Supporting information), tumors in control group and US group grew rapidly. Mice treated with MPB, MPB + US and MPBC showed moderate tumor inhibition. Notably, the MPBC + US group displayed effective tumor growth inhibition owing to the combined effect of catalysis-enhanced SDT and CDT. The effective therapeutic effect of combined therapy was observed by the TUNEL staining of tumors (Fig. 4e). Meanwhile, we also performed hypoxia inducible factor HIF-1α (HIF-1α) and vascular endothelial growth factor (VEGF) staining assay to observe whether the MPB had the ability to relieve hypoxia within tumor. As displayed in Figs. 4f and g, the control group showed strong HIF-1α and VEGF fluorescence, suggesting the hypoxia state of the tumor. MPB group showed weak fluorescence, which was because Pt NPs could catalyze the decomposition of H_2O_2 to produce O_2. Moreover, after different treatments, no obvious damage in the main organ tissues of mice was observed by H&E staining and the body weights of mice had no loss (Fig. S8 in Supporting information and Fig. 4b). Besides, we also performed the serum biochemistry and blood hematological analysis of MPBC + US-treated mice and healthy mice. In Fig. S9 (Supporting information), all the measured parameters between MPBC + US group and healthy group remained in the normal range. Meanwhile, the hemolysis rate of nanoparticle was less than 5% at different concentrations (Fig. S10 in Supporting information). These results demonstrate that the MPBC-based synergistic therapy has good therapeutic effect and a high therapeutic biosafety, which offer an expansive prospect for cancer treatment.

It is reported that Mn-O bonds can be destroyed at faintly acidic and reducing environments [55,56]. Enlightened by this, the release behavior of Mn from MPB at different conditions was explored (Fig. 4d). Compared with pH 7.4, the release rate in acidic (pH 6.5) or reduced (pH 7.4, GSH 10 mmol/L) solution increased significantly, which was due to the fracture of Mn-O bond and the subsequent destruction of $MnSiO_3$ structure. The released Mn^{2+} can be employed for T_1-weighted MRI. Therefore, we explored the potential application of MPB nanocomposites for MRI. As shown in Figs. 4c and i, the longitudinal relaxivities (r_1) of MPB in mildly acidic (pH 6.5) or reduced (pH 7.4, GSH 10 mmol/L) environment was higher than that in neutral (pH 7.4) environment, confirming the pH/GSH-activatable MRI. Moreover, the *in vivo* MRI of the tumor site was also performed. As displayed in Fig. 4h, after intratumoral injection of MPB, the T_1-MR signal of the tumor enhanced. The above results confirm that the MPB is a promising potential MRI agent.

In conclusion, multifunctional MPBC nanoplatforms were constructed to achieve MRI image-guided synergistic SDT/CDT. Under US irradiation, Ce6 could generate ROS for SDT to induce cancer cells apoptosis. And the SDT effect was enhanced by the O_2 in TME generated by the catalase-like activity of the loaded Pt. The

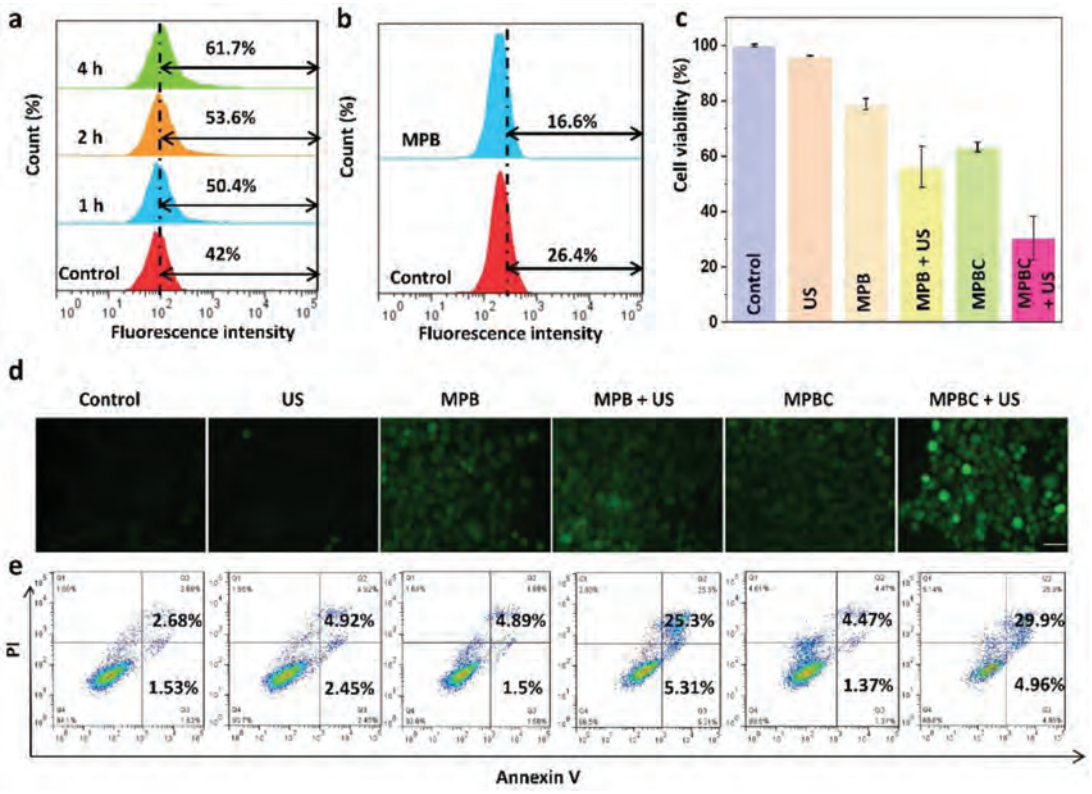

Fig. 3. (a) Cellular uptake of MPBC by HeLa cells at different time points by FCM. (b) Intracellular O_2 change after different treatments probed with O_2 probe $[Ru(dpp)_3]Cl_2$ by FCM. (c) Cell viabilities of HeLa cells after treated with different materials (100 ppm) upon US irradiation (1.0 MHz, 1.5 W/cm^2, 50% duty cycle, 1 min). (d) Intracellular ROS detection of HeLa cells after treated with different conditions. Scale bar is 10 μm. (e) Apoptosis assay of HeLa cells after different treatments by FCM.

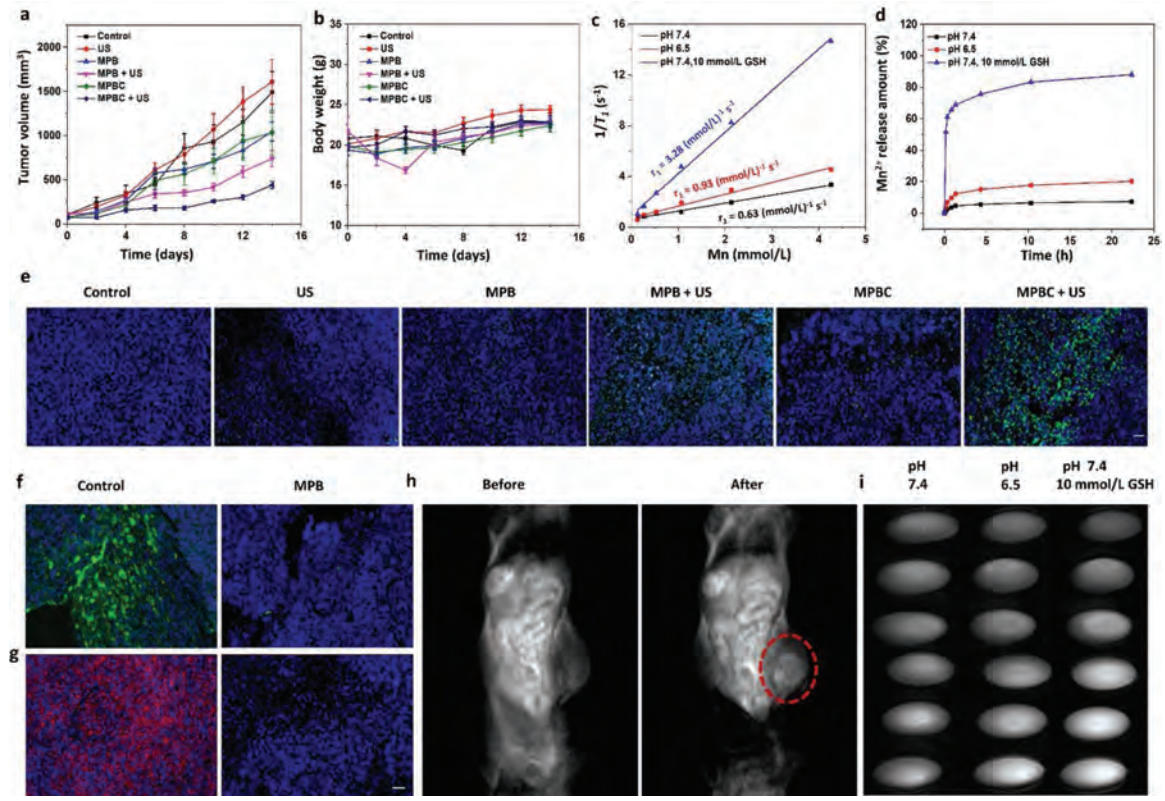

Fig. 4. (a) Tumor-volume curves and (b) body-weight curves of mice after different treatments. (c) Plots of $1/T_1$ *vs.* Mn concentration. (d) The release of Mn in different environments. (e) TUNEL staining in the tumor site of mice after different treatments. (f) HIF-1α and (g) VEGF immunofluorescence images of tumor slices in control and MPB groups. (h) *In vivo* T_1-weighted MRI after the intratumoral injection of MPB. (i) *In vitro* T_1-weighted MRI with different concentrations of MPB (15.625, 31.25, 62.5, 125, 250, 500 ppm) in different environment. Scale bar is 50 μm.

$MnSiO_3$ nanosphere can be degrade in TME, the released Mn^{2+} could catalyze H_2O_2 to produce •OH for CDT and display an excellent potential for T_1-weighted MRI. More importantly, *in vitro* and *in vivo* data showed MPBC-based combined therapy could kill tumor safely and effectively, which supplied a new paradigm in cancer treatment.

Declaration of competing interest

The authors declare that they have no known competing financial interests or personal relationships that could have appeared to influence the work reported in this paper.

Acknowledgments

This work is financially supported by the National Natural Science Foundation of China (NSFC, Nos. 51720105015, 51972138, 51929201, 51922097, 51772124 and 51872282), the Science and Technology Cooperation Project between Chinese and Australian Governments (No. 2017YFE0132300), the Key Research Program of Frontier Sciences, CAS (No. YZDY-SSW-JSC018). All animals experiments in this study were performed according to a protocol approved by the Institutional Animal Care and Use Committee of Jilin University.

Supplementary materials

Supplementary material associated with this article can be found, in the online version, at doi:10.1016/j.cclet.2021.12.096.

References

[1] J.C. Ge, M.H. Lan, B.J. Zhou, et al., Nat. Commun. 5 (2014) 4596.
[2] X.X. Han, J. Huang, X.X. Jing, et al., ACS Nano 12 (2018) 4545–4555.
[3] M.S. Yavuz, Y.Y. Cheng, J.Y. Chen, et al., Nat. Mater. 8 (2009) 935–939.
[4] B.B. Ding, S. Shao, C. Yu, et al., Adv. Mater. 30 (2018) 1802479.
[5] Y.J. Kim, J.H. Ha, Y.J. Kim, Nanotechnology 32 (2021) 275101.
[6] G.L. Fan, F.A. Deng, X. Zhou, et al., Biomaterials 273 (2021) 120854.
[7] Y.Q. Wu, J. Wu, W.Y. Wong, Biomater. Sci. 9 (2021) 4843–4853.
[8] P. Zheng, B.B. Ding, Z.Y. Jiang, et al., Nano Lett. 21 (2021) 2088–2093.
[9] J. An, Y.G. Hu, K. Cheng, et al., Biomaterials 234 (2020) 119761.
[10] S. Bai, N.L. Yang, X.W. Wang, et al., ACS Nano 14 (2020) 15119–15130.
[11] F.L. Gao, G.L. He, H. Yin, et al., Nanoscale 11 (2019) 2374–2384.
[12] S. Liang, X.R. Deng, Y. Chang, et al., Nano Lett. 19 (2019) 4134–4145.
[13] S. Liang, X.R. Deng, G.Y. Xu, et al., Adv. Funct. Mater. 30 (2020) 1908598.
[14] C. Li, X.Q. Yang, J. An, et al., Theranostics 10 (2020) 867–879.
[15] S.T. Gao, P.L. Zheng, Z.H. Li, et al., Biomaterials 178 (2018) 83–94.
[16] Z.X. Xie, S. Liang, X.C. Cai, et al., ACS Appl. Mater. Interfaces 11 (2019) 31671–31680.
[17] C.X. Sui, R. Tan, Y.W. Chen, et al., Bioconjug. Chem. 32 (2021) 318–327.
[18] C.L. Modery-Pawlowski, L.L. Tian, V. Pan, A.S. Gupta, Biomacromolecules 14 (2013) 939–948.
[19] L. Duan, X.H. Yan, A.H. Wang, Y. Jia, J.B. Li, ACS Nano 6 (2012) 6897–6904.
[20] D.A. Belcher, A. Lucas, P. Cabrales, A.F. Palmer, Sci. Rep. 10 (2020) 11372.
[21] J. Yang, W. Li, L.H. Luo, et al., Biomaterials 182 (2018) 145–156.
[22] Y.F. Zhang, Y.Y. Liao, Q.A. Tang, J. Lin, P. Huang, Angew Chem. Int. Ed. 60 (2021) 10647–10653.
[23] L.T. Meng, C.R. Wang, Y.P. Lu, et al., ACS Appl. Mater. Interfaces 13 (2021) 11657–11671.
[24] H.R. Wang, Y.F. Guo, C. Wang, et al., Biomaterials 269 (2021) 120621.
[25] M. Wang, M.Y. Chang, Q. Chen, et al., Biomaterials 252 (2020) 120093.
[26] C. Liu, J. Xing, O.U. Akakuru, et al., Nano Lett. 19 (2019) 5674–5682.
[27] J. Ming, T.B. Zhu, W.H. Yang, et al., ACS Appl. Mater. Interfaces 12 (2020) 51249–51262.
[28] C. Zhang, W.H. Chen, L.H. Liu, et al., Adv. Funct. Mater. 27 (2017) 1700626.
[29] Q.Y. Tang, Z.J. Cheng, N. Yang, et al., Biomaterials 205 (2019) 1–10.
[30] W. Pan, B.J. Cui, P. Gao, et al., Chem. Commun. (Camb) 56 (2020) 547–550.
[31] L. Zeng, H. Cheng, Y.W. Dai, et al., ACS Appl. Mater. Interfaces 13 (2020) 233–244.
[32] X.T. Zhou, M. You, F.H. Wang, et al., Adv. Mater. 33 (2021) 2100556.
[33] Z.M. Tian, H.B. Liu, Z.X. Guo, et al., Small 16 (2020) 2004654.
[34] Y.J. Dai, Y.M. Ding, L.L. Li, Chin. Chem. Lett. 32 (2021) 2175–2728.
[35] C.C. Xue, M.H. Li, C.H. Liu, et al., Angew Chem. Int. Ed. 60 (2021) 8938–8947.
[36] Y.J. Zhao, B.B. Ding, X. Xiao, et al., ACS Appl. Mater. Interfaces 12 (2020) 11320–11328.
[37] M. Suo, Z.M. Liu, W.X. Tang, et al., Nanoscale 12 (2020) 23259–23265.
[38] R. Cao, W. Sun, Z. Zhang, et al., Chin. Chem. Lett. 31 (2020) 3127–3130.
[39] M.Y. Chang, M. Wang, M.F. Wang, et al., Adv. Mater. 31 (2019) 1905271.
[40] Y.L. Wang, Z.L. Li, Y. Hu, et al., Biomaterials 255 (2020) 120167.
[41] L.L. Dong, K. Li, D. Wen, et al., Nanoscale 11 (2019) 12853–12857.
[42] S.S. Wan, Q. Cheng, X. Zeng, X.Z. Zhang, ACS Nano 13 (2019) 6561–6571.
[43] J.M. Xiao, G.L. Zhang, R. Xu, et al., Biomaterials 216 (2019) 119254.
[44] Z.Z. Wang, Y. Zhang, E.G. Ju, et al., Nat. Commun. 9 (2018) 3334.
[45] K.C. Liang, H.T. Sun, Z.B. Yang, et al., Adv. Funct. Mater. 31 (2021) 2100355.
[46] T. Jia, Z. Wang, Q.Q. Sun, et al., Small 16 (2020) 2001343.
[47] L. Chen, W. Feng, X.J. Zhou, et al., RSC. Adv. 6 (2016) 13040–13049.
[48] L. Lin, J.T. Yu, H.W. Lu, et al., Chem. Commun. 57 (2021) 1734–1737.
[49] C.Y. Wang, N.Y. Zhao, Y.X. Huang, et al., Chem. Eng. J. 401 (2020) 126100.
[50] Z.Z. Yu, R.X. Lou, W. Pan, N. Li, B. Tang, Chem. Commun. (Camb) 56 (2020) 15513–15524.
[51] M. Wei, J.Y. Lee, F. Xia, et al., Acta Biomater. 126 (2021) 15–30.
[52] Y.Z. Li, H. Zhou, T.T. Li, et al., J. Mater. Chem. B 9 (2021) 2016–2024.
[53] Y. Liu, J.D. Wu, Y.H. Jin, et al., Adv. Funct. Mater. 29 (2019) 1904678.
[54] B.B. Ding, S. Shao, F. Jiang, et al., Chem. Mater. 31 (2019) 2651–2660.
[55] X. Sun, G.L. Zhang, R.H. Du, et al., Biomaterials 194 (2019) 151–160.
[56] B. Liu, Z. Wang, T.Y. Li, et al., ACS Appl. Mater. Interfaces 12 (2020) 45772–45788.